
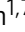










Structural basis of neuropeptide Y signaling through Y₁ receptor

Chaehee Park ^{1,7}, Jinuk Kim ^{1,7}, Seung-Bum Ko¹, Yeol Kyo Choi ², Hyeongseop Jeong ³, Hyeonuk Woo⁴, Hyunook Kang ¹, Injin Bang ^{1,6}, Sang Ah Kim^{1,5}, Tae-Young Yoon ^{1,5}, Chaok Seok ⁴, Wonpil Im ² & Hee-Jung Choi ¹✉

Neuropeptide Y (NPY) is highly abundant in the brain and involved in various physiological processes related to food intake and anxiety, as well as human diseases such as obesity and cancer. However, the molecular details of the interactions between NPY and its receptors are poorly understood. Here, we report a cryo-electron microscopy structure of the NPY-bound neuropeptide Y₁ receptor (Y₁R) in complex with G₁₁ protein. The NPY C-terminal segment forming the extended conformation binds deep into the Y₁R transmembrane core, where the amidated C-terminal residue Y36 of NPY is located at the base of the ligand-binding pocket. Furthermore, the helical region and two N-terminal residues of NPY interact with Y₁R extracellular loops, contributing to the high affinity of NPY for Y₁R. The structural analysis of NPY-bound Y₁R and mutagenesis studies provide molecular insights into the activation mechanism of Y₁R upon NPY binding.

¹Department of Biological Sciences, Seoul National University, Seoul 08826, Republic of Korea. ²Departments of Biological Sciences and Chemistry, Lehigh University, Bethlehem, PA 18015, USA. ³Center for Electron Microscopy Research, Korea Basic Science Institute, Chungcheongbuk-do 28119, Republic of Korea. ⁴Department of Chemistry, Seoul National University, Seoul 08826, Republic of Korea. ⁵Institute for Molecular Biology and Genetics, Seoul National University, Seoul 08826, Republic of Korea. ⁶Present address: Perlmutter Cancer Center, New York University Langone Health, and Department of Biochemistry and Molecular Pharmacology, New York University School of Medicine, New York 10016 NY, USA. ⁷These authors contributed equally: Chaehee Park, Jinuk Kim. ✉email: choihj@snu.ac.kr

The human neuropeptide Y (NPY) system comprises three peptide ligands, NPY, peptide YY (PYY), and pancreatic polypeptide (PP), and four functional NPY receptors Y₁R, Y₂R, Y₄R, and Y₅R¹. These endogenous peptide ligands consisting of 36 amino acids with the amidated C-terminus activate specific NPY receptors generally coupled to G_i or G_o protein². Of these three peptide ligands, NPY, a highly abundant peptide ligand in the brain, can activate all four subtypes of the NPY receptor and is involved in various physiological processes such as food intake, stress response, anxiety, and memory retention^{3–5}. Furthermore, NPY signaling is involved in human diseases such as obesity, mood disorders, and cancers^{6–8}.

The nuclear magnetic resonance (NMR) structure of NPY reveals that its C-terminal segment (13–36) forms an amphipathic α -helix, and the remaining N-terminal part is unstructured and flexible^{9,10}. Previous functional assays using the N-terminal truncation mutants of NPY indicate that the complete N-terminus of NPY is necessary for G_i signaling through Y₁R but not through Y₂R, which shares approximately 30% sequence identity with Y₁R^{10,11}. Similarly, PYY, highly homologous to NPY, binds to Y₁R and Y₂R in its full-length form; however, PYY (3–36), the N-terminal cleaved form found in the circulation, binds only to Y₂R^{12–14}.

NPY receptors belong to the β subgroup of class A G protein-coupled receptors (GPCRs). Among them, Y₁R is expressed in the central nervous system (CNS) as well as in the adipose tissue and vascular smooth muscle cells, where it leads to enhanced cell proliferation and the induction of food intake upon activation by NPY^{15–17}. Thus, the Y₁R antagonist has been proposed as a potential drug for treating obesity¹⁶. Furthermore, Y₁R is highly expressed in human primary breast cancer, implying the utility of Y₁R as a diagnostic marker for breast cancer¹⁸.

The crystal structures of the small molecule antagonist-bound Y₁R have been published recently¹⁰. Although these structures provide molecular details of Y₁R-selective antagonist binding and the overall architecture of an inactive state of Y₁R, the molecular mechanism of its activation by binding of the endogenous agonist NPY is still unknown.

Here, we present a single-particle cryo-electron microscopy (cryo-EM) structure of NPY-bound wild-type Y₁R with G₁₁ protein coupled. The structure reveals that five amino acids at the C-terminus of NPY form an extended conformation and are inserted into a pocket formed by the transmembrane (TM) domain of Y₁R. In addition, the helical region and N-terminus of NPY are shown to be involved in Y₁R binding. Together with molecular dynamics (MD) simulations and functional analysis of various mutations, our structure provides molecular details of endogenous peptide recognition by Y₁R and suggests the activation mechanism of Y₁R upon NPY binding.

Results

Structure determination of the NPY–Y₁R–G₁₁ complex. The published antagonist-bound crystal structure of Y₁R was solved using a modified construct involving thermostabilizing mutation, C-terminal truncation, and replacement of intracellular loop 3 (ICL3) with T4 lysozyme¹⁰. In our study, we used the wild-type Y₁R construct (2–384) with minimal engineering (such as affinity tag) to solve the receptor structure, thereby facilitating molecular analysis of the activation mechanism of the native receptor. Y₁R is known to couple G₁₁ protein to activate downstream signaling upon NPY binding². Before purifying the NPY–Y₁R–G₁₁ complex, we confirmed the functionality of the synthesized NPY by performing bioluminescence resonance energy transfer (BRET) assays, which showed that Y₁R specifically recruited G₁₁ in response to NPY binding (Supplementary Fig. 1). For the

structural study, Y₁R and G₁₁ heterotrimer were purified separately and mixed in the presence of NPY. The complex was incubated with apyrase to obtain a nucleotide-free G₁₁ heterotrimer, and single-chain variable fragment termed scFv16, that specifically recognizes heterotrimeric G_i was added as a stabilizer¹⁹ (Supplementary Fig. 2).

We determined a cryo-EM structure of the NPY–Y₁R–G₁₁–scFv16 complex at a nominal resolution of 3.2 Å in glyco-diosgenin (GDN) micelles (Supplementary Table 1 and Supplementary Fig. 3). Similar to other structures of nucleotide-free G protein heterotrimers bound to GPCR, the α -helical domain of G₁₁ was not modeled in our structure because of its flexibility. Inspection of the cryo-EM map clearly showed the density of NPY protruding into the extracellular region (Fig. 1a). To further focus on the binding of NPY to Y₁R, we subtracted the heterotrimeric G protein signal and subjected to local refinement (Supplementary Fig. 3) as used in the cryo-EM analysis of secretin-bound secretin receptor–G_s complex²⁰. The resulting cryo-EM map allowed modeling of the five residues at the N-terminus (1–5) and the C-terminal half of NPY (20–36) (Fig. 1b, c and Supplementary Fig. 4).

Overall structure of NPY-bound Y₁R receptor. Structural comparison of the NPY-bound and antagonist-bound Y₁R reveals distinct conformational changes in the extracellular region, TM core, and cytoplasmic part of the receptor upon activation. As the amidated C-terminus of NPY penetrates deep into the TM core, the extracellular tips of TM3, TM4, TM6, and TM7 slightly move outward by 1.9–2.5 Å in the NPY-bound Y₁R structure compared to the antagonist-bound structure, opening up the ligand-binding pocket (Fig. 2a). In fact, the calculated solvent-accessible ligand-binding cavities in the antagonist-bound and NPY-bound structures are ~506 and 730 Å³, respectively (Supplementary Fig. 5). Besides the interaction of the C-terminal tail of NPY with the Y₁R TM core, the molecular interaction of the remaining NPY with Y₁R was difficult to characterize, as the NPY map was not well resolved (Supplementary Fig. 3). However, we could observe the density of the N-terminal and helical regions of NPY, which are surrounded by extracellular loops (ECLs) and the N-terminal region of Y₁R (Supplementary Fig. 6). ECL2, ECL3, and the N-terminal region of Y₁R directly interact with NPY to varying degrees. The details of the NPY interaction are discussed later.

NPY binding results in the TM core of Y₁R undergoing conventional conformational changes associated with the activation mechanism of class A GPCRs. Immediately below the C-terminus of NPY peptide, side chains of I128^{3,40}, P223^{5,50}, and F272^{6,44} (superscripts are the Ballesteros–Weinstein numbers²¹) in the connector region are repacked to contract the interface of TM3, 5, and 6 (Fig. 2b), resulting in the outward movement of TM6 and inward movement of TM7 at the cytoplasmic part of Y₁R (Fig. 2a). In addition, R138^{3,50} of the (D/E)R(Y/H) motif makes close contact with Y231^{5,58} and Y320^{7,53} of the NPxxY motif (Fig. 2c), a well-known key interaction observed in the activated GPCR structures. These conformational changes demonstrate that our structure represents the active conformation of class A GPCRs.

Compared to other G₁₁-bound class A GPCRs, such as neurotensin receptor 1 (NTSR1) and μ -opioid receptor (μ OR), Y₁R has a relatively short ICL2, comprising six amino acids, including two Pro residues (Fig. 2d). In NTSR1 and μ OR, ICL2s adopt an α -helix upon activation, interacting with the α N, α N- β 1 loop and α 5 helix of G₁₁^{22,23}. In contrast, ICL2 of Y₁R remains as a loop in the G₁₁-bound state, forming contacts with only the α 5 helix of G_i through R146^{ICL2} and R149^{ICL2} (Fig. 2d). In addition to ICL2, hydrophobic residues in TM3, TM5, and TM6 (I142^{3,54}, I234^{5,61}, L238^{5,65}, I261^{6,33}, and L265^{6,37}) of Y₁R form van der

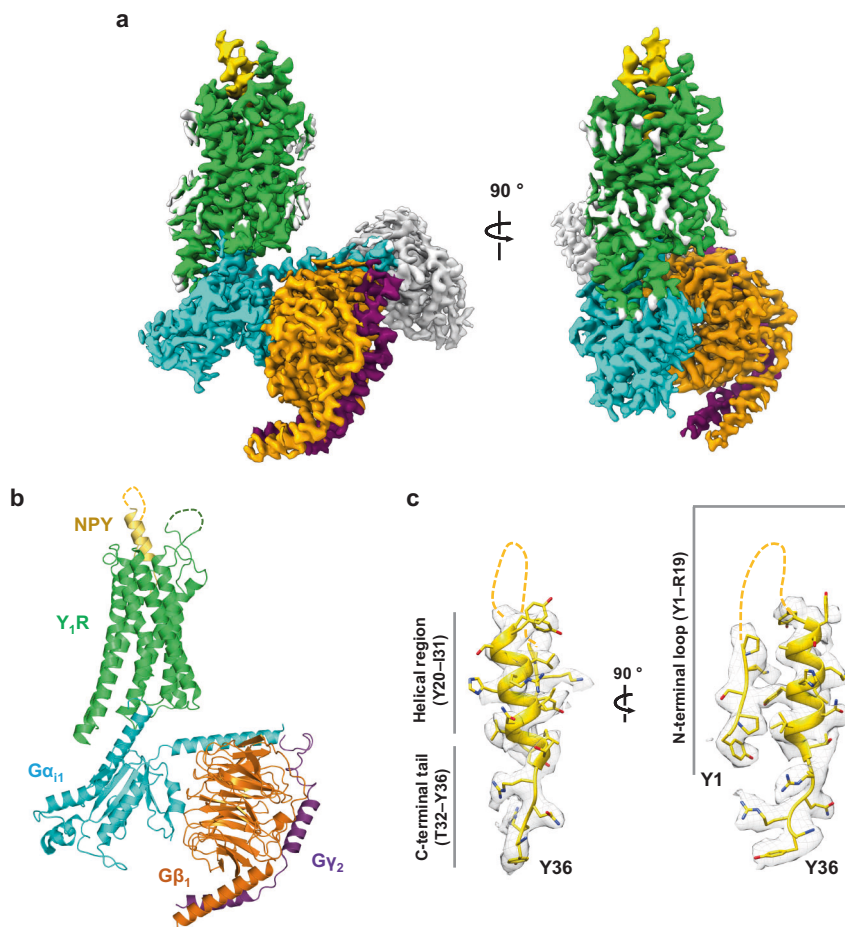


Fig. 1 Overall structure of the NPY- Y_1R - G_{i1} -scFv16 complex. **a** The cryo-EM map of the NPY- Y_1R - G_{i1} -scFv16 complex is shown. Y_1R , NPY, $G_{\alpha_{11}}$, G_{β_1} , G_{γ_2} , and scFv16 are colored green, yellow, cyan, orange, purple, and gray, respectively. The remaining micelle density is shown in light gray. Details on cryo-EM map generation are described in the “Methods” section. **b** The structure of the NPY- Y_1R - G_{i1} complex is shown. scFv16 is included in the final structure but omitted in this figure for clarity. **c** The sharpened cryo-EM map with the NPY peptide model is shown in two orientations. NPY residues 6–19 are not modeled in this structure and are shown as dashed lines. The three regions of NPY are marked as the N-terminal loop region (Y1–R19), the helical region (Y20–I31), and the C-terminal tail (T32–Y36).

Waals interactions with L348 and L353 in the α_5 helix of G_{i1} (Supplementary Fig. 7) and R260^{6,32} of Y_1R forms polar interaction with the carboxyl group of F354 in the α_5 helix of G_{i1} (Supplementary Fig. 7). Most of these interactions are conserved in the hNTSR1- G_{i1} and μ OR- G_{i1} structures (Supplementary Fig. 7). However, when aligning the receptors, the relative position of the α_5 helix of G_{i1} bound to Y_1R slightly differs by ~ 2 Å displacement of the C-terminus of $G_{\alpha_{11}}$ or $\sim 8^\circ$ tilt angle of the α_5 helix of G_{i1} in the NTSR1-bound and μ OR-bound G_{i1} structures, respectively (Supplementary Fig. 7).

Binding of the C-terminal tail of NPY to Y_1R . Our cryo-EM map shows a well-resolved density for the five C-terminal residues of NPY (32–36) (Fig. 1c), forming an extended structure, contrasting the α -helix formation of residues 13–36 in the NMR structure of human NPY (PDB ID 1RON)⁹. However, helix unwinding at the C-terminal tail of NPY was not unexpected since the previous NMR study of porcine NPY bound to Y_1R suggested an extended conformation of the NPY C-tail¹⁰. Similarly, the nine amino acids at the C-terminus of orexin-B neuropeptide (OxB) were previously shown to form an extended conformation in the orexin receptor (OX_2R)-bound state but form an α -helix in the receptor-free state^{24,25}.

The extended conformation of the NPY C-tail binds to a pocket lined by TM helices 2–7, with a depth of ~ 11 Å from the top surface of the membrane (Fig. 3a, b). It is well established that the amidation of NPY C-terminal tyrosine is critical for its function; consistently, in this study, non-amidated NPY failed to elicit G protein signaling (Supplementary Fig. 8). At the bottom of the ligand-binding pocket, the C-terminal amide of NPY points toward the side chain of Q120^{3,32} (Fig. 3c), which has been predicted to interact with the Y36 side chain in the NPY-docked Y_1R model¹⁰. The importance of Q120^{3,32} for G_i recruitment and signaling upon NPY treatment was investigated using BRET and calcium signaling assays. As expected, the Q120^{3,32}A mutant exhibited reduced $G_{\alpha_{11}}$ recruitment and an increased EC_{50} (Supplementary Table 2 and Supplementary Figs. 9, 10, and 11). The C-terminal amide of Y36 is further coordinated by H306^{7,39} through polar interactions and C93^{2,57} and M310^{7,43} through van der Waals contacts (Fig. 3c). Furthermore, the ligand-binding pocket of Y_1R is highly acidic (Supplementary Fig. 12). The acidic residues of the binding pocket repel the negatively charged C-terminus and favor the amidated C-terminus. A similar acidic patch in the ligand-binding pocket is observed in OX_2R , where the amidated C-terminus of OxB binds. In contrast, the ligand-binding pocket is basic in NTSR1 and endothelin B receptor (ET_{BR}), whose peptide agonists have the C-terminal carboxyl groups (Supplementary Fig. 12).

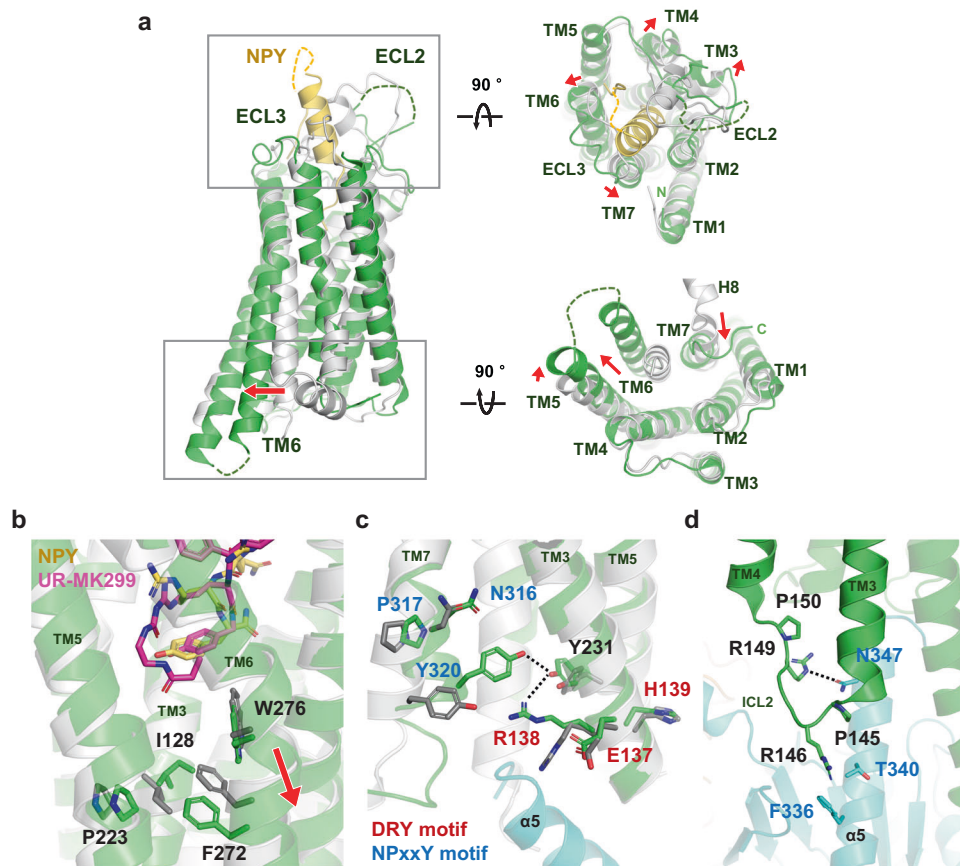


Fig. 2 Comparison between NPY-bound and antagonist-bound Y₁R structures. **a** Structural alignment between NPY (yellow)-bound Y₁R (current structure, green) and antagonist-bound Y₁R (PDB ID 5ZBQ, light gray, residues 18–32 of Y₁R and antagonist are omitted for clarity) clearly shows characteristic TM6 movement as observed in the active structures of class A GPCRs. Views from extracellular (right-upper panel) and cytoplasmic (right-lower panel) sides are shown on the right. Each red arrow represents the movement of the TM helix. **b** Structural changes at the connector region (p5.50|3.40f6.44 motif) upon NPY binding are shown. The antagonist-bound Y₁R (PDB ID 5ZBQ) is colored in light gray and an antagonist, UR-MK299, in magenta. **c** Structural changes at the D(E)/R/Y(H) (labeled in red) and NPxxY (labeled in blue) motifs are shown. **d** The binding interface between $\alpha 5$ of G₁₁ (in cyan) and ICL2 is shown. Residues participating in the interactions and two Pro residues (P145^{ICL2} and P150^{ICL2}) in ICL2 are shown as sticks. Dashed lines represent the polar interactions.

The Y36 side chain of NPY forms a hydrogen bond with Q219^{5,46} through its hydroxyl group and hydrophobic interaction with I124^{3,36} through its phenyl ring (Fig. 3c). The importance of Q219^{5,46} and I124^{3,36} for NPY signaling was demonstrated by 13.5-fold and 3.5-fold reduction in NPY potency in the Q219^{5,46}A and I124^{3,36}A mutants, respectively¹⁰. Previous mutational studies of NPY showed that the Y36F mutation had a relatively mild effect on Y₁R binding²⁶. In contrast, the Y36A mutation caused a loss of binding to Y₁R^{10,26}, suggesting that the phenyl ring of Y36 is more important for NPY signaling. Our structure shows that the phenyl ring of Y36 forms an intramolecular interaction with R35 of NPY (Supplementary Fig. 13), which aids in correctly positioning R35, in addition to hydrophobic interactions with Y₁R (Fig. 3a).

R33 and R35 of NPY extensively interact with the Y₁R TM core, and alanine scanning mutagenesis of NPY has shown that R33A and R35A mutations of NPY exhibit the most severe defects in Y₁R binding^{10,26}. R33 of NPY forms a hydrogen bond with N283^{6,55} and π -cation interactions with F286^{6,58} and F302^{7,35} (Fig. 3d). BRET analysis using the N283^{6,55}A mutant showed a dramatic decrease in G_q recruitment and reduced NPY potency by 85-fold compared to wild-type Y₁R (Supplementary Table 2 and Supplementary Figs. 9, 10, and 11). Previous mutagenesis studies of F286^{6,58} and F302^{7,35} showed that substituting of these residues with alanine caused a reduction in

NPY potency^{10,27}. R35 forms electrostatic interaction with D287^{6,59} and van der Waals interaction with F173^{4,60}, both of which have been reported to be essential for NPY signaling^{10,28}.

Q34 and T32 of NPY are oriented opposite to the R35 and R33 side chains, interacting with T97^{2,61}, Y100^{2,64}, and the backbone carbonyl of D104^{2,68} (Fig. 3e). In particular, Y100^{2,64} is sandwiched between T32 and Q34, forming nonpolar contacts with both (Fig. 3e). Consistent with these structural data, Y100^{2,64}A, a well-known mutation, dramatically decreased downstream NPY signaling^{10,27,28}. In the antagonist-bound structures, none of these residues that interact with T32 and Q34 are involved in antagonist binding.

Altogether, our structural analysis shows that the C-terminal tail of NPY forms extensive interactions with Y₁R residues on TM2, 3, 5, and 6. Previous and current mutational studies support the importance of these interacting residues in NPY signaling.

Structural changes in Y₁R TM core by binding of NPY C-terminal tail.

The binding pocket for the NPY C-terminus is where the two antagonists (UR-MK299 and BMS-193885) bind in the previously reported inactive Y₁R structures. The structural comparison reveals that the hydroxyphenyl group and guanidine moiety of UR-MK299 exhibit binding modes similar to those of the side chains of Y36 and R35 of NPY, respectively, making polar interactions with Q219^{5,46} and D287^{6,59} (Fig. 4a). The BMS-

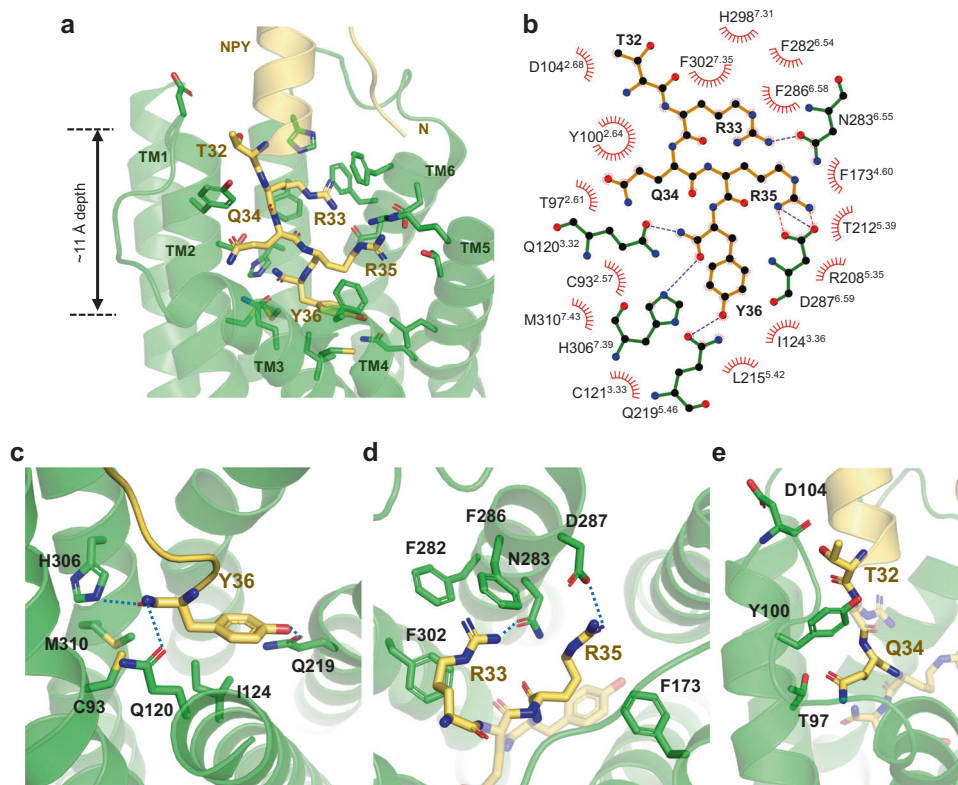


Fig. 3 Binding of NPY C-terminal tail to Y_1R . **a** The C-terminal tail of NPY (yellow) and Y_1R residues that participate in NPY binding are presented as sticks. **b** Schematic representation of NPY- Y_1R interactions analyzed using the LigPlot+ program is shown. The hydrogen bonds and the salt bridges are shown in blue and red dashed lines, respectively. **c-e** Detailed interactions between C-terminal residues of NPY and Y_1R are shown. The polar contacts are shown as blue dashed lines.

193885-bound inactive Y_1R structure shows that D287^{6.59} of Y_1R interacts with the antagonist, whereas Q219^{5.46} of Y_1R is not involved in this antagonist binding, as Q219^{5.46} is pushed away by the dihydropyridine group (Fig. 4b). In both inactive structures, Q120^{3.32} makes van der Waals contact with M310^{7.43}, although Q120^{3.32} rotamers differ in two inactive structures, forming polar interaction with BMS-193885 or van der Waals interaction with W276^{6.48} (Fig. 4c). In the NPY-bound Y_1R structure, the Q120^{3.32} sidechain adopts an upward-facing rotamer, forming a polar contact with the amidated C-terminus. Also, Q120^{3.32} no longer interacts with M310^{7.43} (>7 Å) but with C93^{2.57}. Reorganization of interaction network near Q120^{3.32} by NPY binding stabilizes the conformation of the upward displacement of TM3 (Fig. 4c).

The hydrophobic moieties of the antagonists form hydrophobic networks with I124^{3.36}, I128^{3.40}, F272^{6.44}, W276^{6.48}, and L279^{6.51} at the bottom of the ligand-binding pocket and with F282^{6.54}, F286^{6.58}, and F302^{7.35} near the entrance to the binding pocket, to stabilize the inactive Y_1R structure. These hydrophobic networks are rearranged in the NPY-bound structure. As mentioned above, at the bottom of the ligand-binding pocket, a rotamer change of I128^{3.40} and repacking of F272^{6.44} and W276^{6.48} occur upon NPY binding (Fig. 2b). The three phenylalanine residues F282^{6.54}, F286^{6.58}, and F302^{7.35} on TM6 and TM7 form a stable π - π network with phenyl groups present in both antagonists; however, this aromatic network is disrupted in the NPY-bound structure. The phenyl ring of F286^{6.58} flips to form van der Waals contact with L30 and a π -cation interaction with R33 of NPY (Fig. 4d). F282^{6.54} and F302^{7.35} form a new interaction network with H298^{7.31} and I293^{ECL3} (Fig. 4e). F286^{6.58} also interacts with Y1 and P2 of NPY. The NPY N-terminus interactions are discussed in the next section.

Comparison of binding modes between the NPY C-terminal tail and antagonists reveals common interactions of the ligand for

Y_1R binding and NPY-specific interactions, providing hints for designing novel Y_1R ligands that bind to the TM core. In addition, the structural comparison of the TM core between inactive and active states of Y_1R suggests the key events of conformational changes during activation by NPY, rearrangement of the hydrophobic network around F286^{6.58} at the entrance to the ligand-binding pocket, and rearrangement of interaction network around Q120^{3.32} and I128^{3.40} in the connector region at the bottom of the ligand-binding pocket.

Binding of the N-terminal and helical regions of NPY to Y_1R .

In the OxB-bound OX₂R structure, the N-terminus of OxB was not observed despite being necessary for signaling. In our complex structure, we were surprised to observe the density of the helical and the N-terminal loop regions of NPY in addition to the C-terminal tail (Fig. 1c). The NPY residues 20–31 were built as an α -helix based on the continuous cryo-EM density from the C-terminus (Fig. 1c and Supplementary Fig. 4). This α -helical region forms relatively loose interactions with ECLs compared to the C-terminal tail of NPY that forms extensive interactions with the TM core. The cryo-EM map density was weaker toward the N-terminus of the helix, suggesting the flexibility of this region. Three independent 1- μ s MD simulations using a model composed of full-length NPY, Y_1R (2–339), and G₁₁ protein showed that the angle of the helical axis of NPY to the membrane normal varied from 5° to 70° during the simulations (Supplementary Fig. 14). While the C-terminal tail of NPY maintained its binding pose during the simulations, the movement increased toward the N-terminus of the NPY helix, explaining the weak density of the N-terminal end of the NPY helix.

The density of side chains in the ECL2 region spanning residues 185–193 was unclear, but we identified that P183^{ECL2},

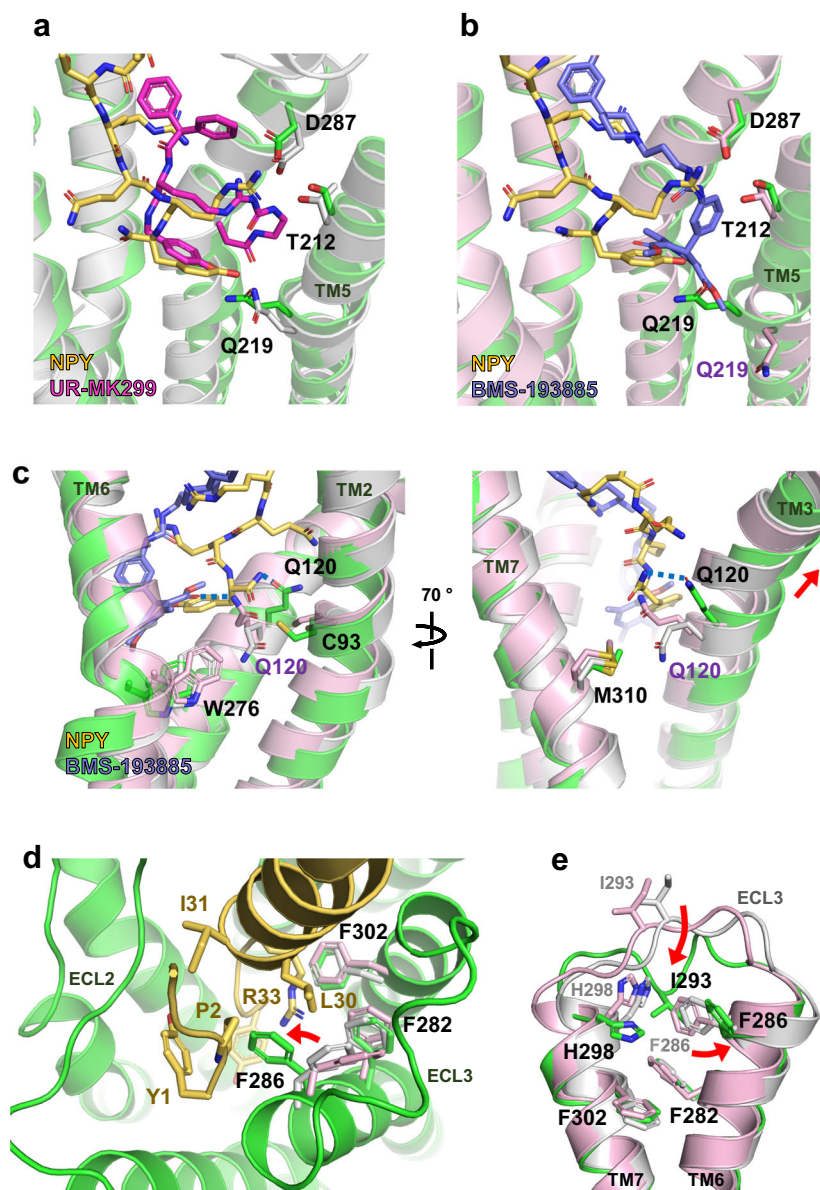


Fig. 4 Comparison of binding mode between NPY and antagonists. **a** Ligand-binding site occupied by UR-MK299 (PDB ID 5ZBQ, magenta) and **b** BMS-193885 (PDB ID 5ZBH, slate) is compared with the binding site for NPY (yellow). The side chains of Q219^{5,46} are differently oriented in all three structures, whereas D287^{6,59} and T212^{5,39} maintain similar interactions. **c** Q120^{3,32}-mediated interactions in the antagonist-bound and NPY-bound structures are compared. In the NPY-bound active structure of Y₁R, TM3 including Q120^{3,32} shifts upward and Q120^{3,32} forms a polar interaction with the C-terminal amide of NPY through its upward-facing sidechain. **d** Upon NPY binding, F286^{6,58} rotamer is changed to form the interactions with NPY R33, L30, and Y1. **e** Upon NPY binding, I293^{ECL3} participates in a hydrophobic interaction network with F286^{6,58}, H298^{7,31}, and F302^{7,35}. UR-MK299-bound Y₁R is indicated in light gray, and BMS-193885-bound Y₁R is in pink. Red arrows represent positional changes of I293^{ECL3} and F286^{6,58} upon NPY binding.

F184^{ECL2}, and F199^{ECL2} interacted with Y27, I28, and I31 of NPY, respectively (Fig. 5a). The F184^{ECL2A} and F199^{ECL2A} mutants reduce the potency of NPY by 38-fold and 2.3-fold, respectively (Supplementary Table 2 and Supplementary Figs. 15, 16, and 17). Although the F202^{ECL2A} mutation exhibited attenuated G protein signaling, F202^{ECL2} did not interact with NPY. F202^{ECL2} appears to be important for maintaining the structural integrity of the receptor by forming an aromatic network with F173^{4,60}, Y176^{4,63}, and Y211^{5,38}, as observed in both inactive and active structures (Supplementary Fig. 18).

Previously, it was proposed that the complete N-terminus of NPY is necessary for NPY signaling through Y₁R¹⁰. Consistently, our signaling assays demonstrated the decrease in the potency of NPY(3–36) and NPY(18–36) by 18-fold and 300-fold,

respectively, compared to full-length NPY (Fig. 5b), suggesting that the N-terminal residues of NPY are important for Y₁R binding. In our structure, NPY residues 1–5 were modeled by fitting these residues into a cryo-EM map (Fig. 1c and Supplementary Fig. 19). Among these five residues, the N-terminal residue Y1 was relatively well defined by the cryo-EM density. Y1 interacts with F199^{ECL2}, D200^{ECL2}, and R208^{5,35} of Y₁R (Fig. 5c), all of which were demonstrated to be important for NPY signaling by previous or current mutational studies^{27,28} (Supplementary Table 2 and Supplementary Figs. 15, 16, and 17).

The N-terminus of NPY does not enter the TM core like the C-terminus but is exposed to the solvent, suggesting its propensity to interact more dynamically with Y₁R. In agreement with our speculation, MD simulations show that the N-terminal

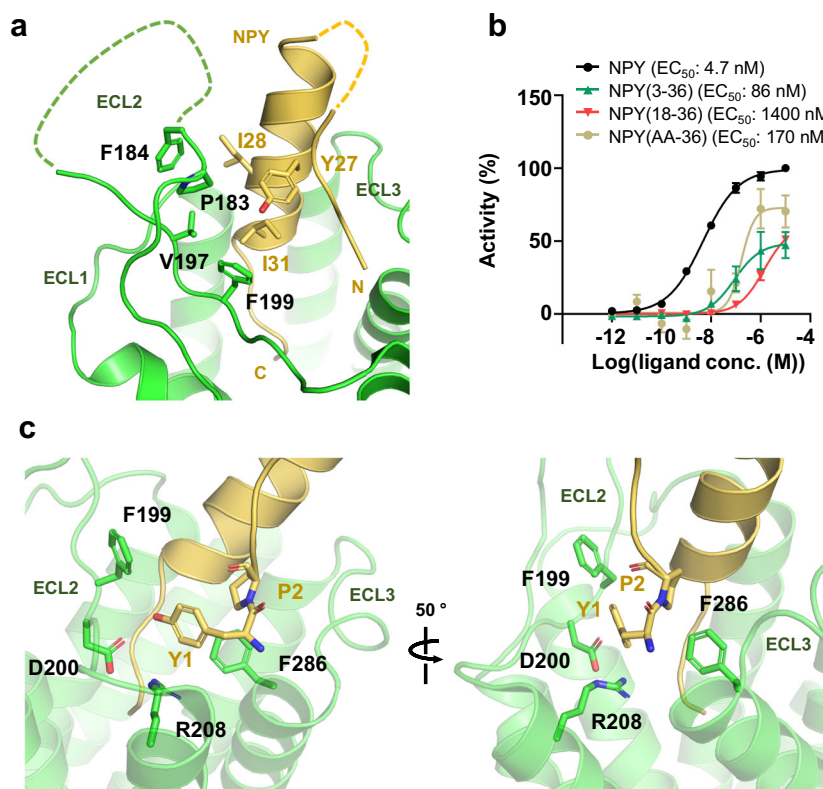


Fig. 5 Binding of NPY N-terminus to Y_1R . **a** The sticks show the residues participating in van der Waals interactions between NPY helix and ECL2 of Y_1R . Unresolved regions of NPY and ECL2 of Y_1R are shown with dashed lines. **b** The results of Ca^{2+} assays performed with N-terminally truncated NPY peptides are shown. Removal of two N-terminal residues dramatically reduces NPY potency and efficacy. Symbol and error bar indicate the mean and S.E.M. (standard error of mean) of $n =$ three (NPY(3-36), NPY(18-36), and NPY(AA-36)) or $n = 17$ (NPY) independent experiments, respectively. Calculated EC_{50} values ($pEC_{50} \pm$ SEM) are presented on each graph and are summarized in Supplementary Table 2. Source data are provided as a Source Data file. **c** Van der Waals interactions of Y1 and P2 of NPY with Y_1R are shown in two different orientations.

region of NPY exhibits relatively higher motions than the C-terminal tail (32–36) during 1- μ s simulation. Moreover, the Y1-mediated interactions were broken and reformed in one of the replicates during the simulations (Supplementary Fig. 14). Collectively, our data show that the N-terminal region of NPY interacts dynamically with Y_1R . Our model structure represents a possible conformation of the NPY N-terminus, deduced from the cryo-EM map.

Functional role of the N-terminal region of Y_1R . Our cryo-EM map reveals a continuous density from the N-terminal end of TM1 toward the NPY ligand (Supplementary Fig. 6), suggesting an interaction between them. Previously, the N-terminal region of Y_1R , residues 21–32, was crosslinked to NPY in a photo-crosslinking experiment¹⁰. However, the low-resolution map at TM1 and the N-terminal region of Y_1R prevented us from unambiguously determining whether the N-terminal region of Y_1R directly interacted with NPY. Through signaling assays and structural analysis, it was previously proven that N-terminal residues were critical for peptide ligand binding and activation of other closely related peptide receptors, namely OX_2R and $ET_B R$ ^{29–32}.

To validate the importance of the N-terminal region of Y_1R for NPY signaling, we constructed two N-terminal deletion mutants of Y_1R , one in which the 25 N-terminal residues were deleted ($Y_1R\Delta 25$) and the other in which the 31 N-terminal residues were deleted ($Y_1R\Delta 31$), and performed BRET and Ca^{2+} assays (Supplementary Table 2 and Supplementary Figs. 20, 21, and 22). $Y_1R\Delta 25$ behaves like wild-type Y_1R in recruiting G_{i1} by NPY

treatment, whereas $Y_1R\Delta 31$ showed attenuated response to NPY; this finding suggests that residues 26–31 are involved in NPY binding and thus in G_{i1} recruitment. In particular, the hydrophobic residues $L26^N$ and $F28^N$ in Y_1R were important for NPY signaling, as indicated by the 2.8-fold increase in EC_{50} in the $L28^N A/F28^N A$ mutant (Supplementary Table 2 and Supplementary Figs. 20, 21, and 22). MD simulations show that although the N-terminal region of Y_1R has high mobility, $L26^N$ and $F28^N$ are within the Ca distance of 9 and 13 Å, respectively, from Y21 in the helical region of NPY (Supplementary Fig. 23). Of note, Y21 of NPY is assumed to be a contact point based on the nearby extra cryo-EM density. In addition, the helical region of NPY was demonstrated to interact with ECL2 during the simulations, suggesting that ECL2 and the N-terminal region of Y_1R form dynamic interactions with NPY by reorienting themselves extensively to accommodate the NPY binding (Supplementary Fig. 23). Thus, we hypothesize that the helical region of NPY forms a tripartite interaction with ECL2 and the N-terminal region of Y_1R , both are shown to partially cover the ligand-binding pocket in the antagonist-bound Y_1R structures.

Discussion

Several structures of the G protein-bound active state of class A GPCRs in complex with endogenous peptide agonists, such as NTS (8–13), $Ox B$, and cholecystokinin-8 (CCK-8), have been reported^{24,33,34}. Commonly, these peptide agonists have a C-terminal region that inserts into the receptor TM core and acts as a “message” domain (Supplementary Fig. 24)^{35,36}. Similarly, in this study, we observed that the five NPY C-terminal residues in

the NPY-bound Y₁R structure, forming an extended conformation, make extensive contact with residues in the TM core. In addition, our structure shows that the helical region and the N-terminal loop of NPY interact with Y₁R, although this interaction is much more dynamic and even transient, as indicated by the weaker density for this region in our cryo-EM map, as well as our MD simulations. This study presents a model candidate containing the five N-terminal residues of NPY, constructed based on our cryo-EM map. The cryo-EM density for Y1 of NPY is relatively well resolved, showing interaction with F199^{ECL2}, D200^{ECL2}, and R208^{5.35} of Y₁R. Despite being a dynamic interaction, the NPY N-terminus is crucial for G_i signaling, as demonstrated by reduced G_i recruitment in the BRET assay and a 18-fold increase in EC₅₀ value in signaling assays after treatment with NPY(3–36). The NPY receptor has two other peptide ligands, PYY and PP. PYY is released in response to nutrient intake along the gut and is highly homologous to NPY with 67% sequence identity; its N-terminus starts with tyrosine, similar to NPY (Supplementary Fig. 25). However, the major circulating form of PYY is the cleaved form PYY(3–36), known to be selective for Y₂R^{12,13,37}. Our signaling assays with NPY, PYY, NPY(3–36), and PYY(3–36) also show that Y₁R has EC₅₀ values in the nanomolar range for NPY and PYY (4.7 and 6.1 nM, respectively) and 13–18-fold increased EC₅₀ values for NPY(3–36) and PYY(3–36) (86 nM and 77 nM, respectively) (Supplementary Fig. 26), suggesting that PYY would bind Y₁R similarly to NPY if its N-terminus remains intact. On the contrary, PP is secreted in the pancreas and has 50% sequence identity with NPY (Supplementary Fig. 25). Reportedly, PP does not bind Y₁R at all³⁸. PP has A1 and P34 instead of Y1 and Q34, respectively; thus, the interactions of Y1 and Q34 as shown in our NPY-bound Y₁R structure are important for receptor binding. Indeed, our signaling assay shows that Y₁R has a 64-fold increased EC₅₀ value for PP compared to NPY (Supplementary Fig. 26). Among four subtypes of the NPY receptor, Y₄R was activated in response to PP^{38–40}. Interestingly, Y₄R has Glu at the position of 6.58 (E288^{6.58}), instead of Phe as in Y1R (Supplementary Fig. 27), suggesting that Y₄R would form a charged interaction network with nearby charged residues (E203^{ECL2}, R211^{5.35}, T215^{5.39}, N285^{6.55}, E288^{6.58}, D289^{6.59}) and basic residues of PP, R33 and R35 (Supplementary Fig. 28). We speculate that this extensive charged interaction network would provide sufficient interaction energy for Y₄R to accommodate PP as well as NPY, which should be validated with experimental data.

Unlike the previously predicted NPY binding pose, our structure shows that the C-terminal amide of NPY points toward Q120^{3.32} of Y₁R, and the Y36 side chain interacts with Q219^{5.46}. The importance of Q120^{3.32} and Q219^{5.46} for NPY binding and signaling is demonstrated by the approximately 2 and 4-fold increased EC₅₀ values measured using the mutants Q120^{3.32}A and Q219^{5.46}L, respectively. Notably, the Y36 side chain occupies a position similar to the hydroxyphenyl ring of the antagonist UR-MK299¹⁰. Thus, in both active and inactive structures, Q219^{5.46} forms a hydrogen bond with the hydroxyl group of the hydroxyphenyl ring in each ligand. In contrast, Q120^{3.32} of Y₁R forms a hydrogen bond with the C-terminal amide of NPY; however, it is not involved in antagonist binding. Notably, the conserved Gln residue at position 3.32 in OX₂R (Q134^{3.32}) forms a hydrogen bond with the peptide agonist. Therefore, it was proposed to be a key residue in facilitating the transition to an active state of OX₂R by a rotamer change to its upward-facing extended conformation²⁴. This proposal appears to apply to the Y₁R activation mechanism, as a similar rotamer change of Q120^{3.32} is observed upon activation (Fig. 6).

Comparison of the inactive and active structures suggests the activation mechanism of Y₁R upon NPY binding. In the

published antagonist-bound structures, the three phenylalanine residues F282^{6.54}, F286^{6.58}, and F302^{7.35} located near the entrance to the ligand-binding pocket constitute a hydrophobic cluster with the antagonists UR-MK299 and BMS-193885. Upon NPY binding, R33 of NPY is inserted into this Phe network, causing a rotamer change in F286^{6.58}, disrupting the aromatic network. In association with the conformational change of ECL3, a new interaction network including Y1 and R33 of NPY and F282^{6.54}, F286^{6.58}, F302^{7.35}, I293^{ECL3}, and H298^{7.31} of Y₁R is formed, stabilizing the NPY-bound Y₁R structure (Fig. 4e). At the bottom of the ligand-binding pocket, Y36 of NPY forms hydrophobic interaction with I124^{3.36} through the phenyl group and polar interaction with Q120^{3.32} through the amidated C-terminus, leading to a rotamer change of Q120^{3.32}. This is followed by a rotamer change of I128^{3.40}, which interacts with I124^{3.36} and repacking of the side chains of P223^{5.50}, F272^{6.44}, and W276^{6.48}. A series of these changes upon NPY binding pulls TM3 upward and causes outward movement of the cytoplasmic region of TM6 (Fig. 6).

One of the key NPY-interacting residues, F286^{6.58}, is not conserved and replaced by valine in Y₂R and glutamate in Y₄R, both of which cannot form π -cation interaction with R33 as F286^{6.58} does. The difference in the Phe network may explain the Y₁R selectivity of the two antagonists used to determine the inactive Y₁R structures; additionally, it suggests that Y₁R, Y₂R, and Y₄R may have different interaction networks with NPY. In addition to F286^{6.58}, Q219^{5.46}, which forms a hydrogen bond with Y36, is replaced with L227^{5.46} in Y₂R, and H298^{7.31}, which forms an interaction network with F282^{6.54}, F286^{6.58}, and F302^{7.35} is replaced with G300^{7.31} in Y₄R. It should also be noted that F286^{6.58} is located within a distance of 4–5 Å to Y1 and P2 of NPY. Further details would only be explained by investigating the NPY-bound Y₂R and Y₄R structures in the future. However, the vicinity of the residue and the importance of the Phe network suggest that F286^{6.58} may contribute to the difference between Y₁R and Y₂R in the need for the complete N-terminus to elicit a full response.

Methods

Expression and purification of Y₁R. Wild-type human Y₁R (2–384) with a FLAG tag at its N-terminus as well as eGFP and a His₆ tag at its C-terminus, cleavable by HRV 3C protease, was expressed in *Spodoptera frugiperda* (Sf9) insect cells using the Bac-to-Bac system (Invitrogen). Cells were harvested 48 h after infection and lysed by repeated dounce homogenization with lysis buffer (20 mM HEPES pH 8.0, 150 mM NaCl, and 1 mM EDTA) supplemented with phenylmethylsulfonyl fluoride (PMSF), benzamide, and leupeptin. Y₁R was extracted from the cell membrane using a solubilization buffer consisting of 20 mM HEPES pH 8.0, 150 mM NaCl, 1% (w/v) n-dodecyl- β -D-maltoside (DDM), 0.1% (w/v) cholesterol hemisuccinate (CHS), PMSF, benzamide, and leupeptin. After centrifugation, the supernatant was incubated with Ni-NTA resin for 1 h at 4 °C. After column washing with wash buffer (20 mM HEPES pH 8.0, 150 mM NaCl, 20 mM imidazole, 0.05% DDM, and 0.005% CHS), the bound protein was eluted with 300 mM imidazole and subsequently loaded onto anti-FLAG M1 agarose resin (Sigma Aldrich) in the presence of 2 mM CaCl₂. After column washing and on-column exchange of detergent from DDM to glyco-diosgenin (GDN), the bound protein was eluted with M1 elution buffer (20 mM HEPES pH 8.0, 150 mM NaCl, 0.01% GDN, 0.1 mg/ml FLAG peptide, and 4 mM EDTA). Heterogeneous glycosylation was removed by PNGase F (NEB), and the eGFP was cleaved by the HRV 3C protease (homemade). Y₁R was further purified using a Superdex 200 10/300 gel filtration column (Cytiva) pre-equilibrated with a buffer containing 20 mM HEPES pH 8.0, 150 mM NaCl, and 0.01% GDN. Freshly purified Y₁R was used to form a complex with G_{1i} heterotrimer.

Purification of the G protein. Human G α_{i1} with a His₆ tag at its N-terminus was expressed in *Escherichia coli* (*E. coli*) Rosetta (DE3) cells. Protein expression was induced with 0.5 mM isopropyl β -D-1-thiogalactopyranoside (IPTG), and the cells were harvested after incubation at 25 °C overnight. Cells were lysed with Emulsiflex C3 (Avestin), and the cleared lysate after centrifugation was loaded onto the Ni-NTA column. The column was washed with wash buffer (20 mM Tris-HCl pH 8.5, 150 mM NaCl, 30 mM imidazole), and the bound protein was eluted with elution buffer (20 mM Tris-HCl pH 8.5, 150 mM NaCl, and 300 mM imidazole). A His₆

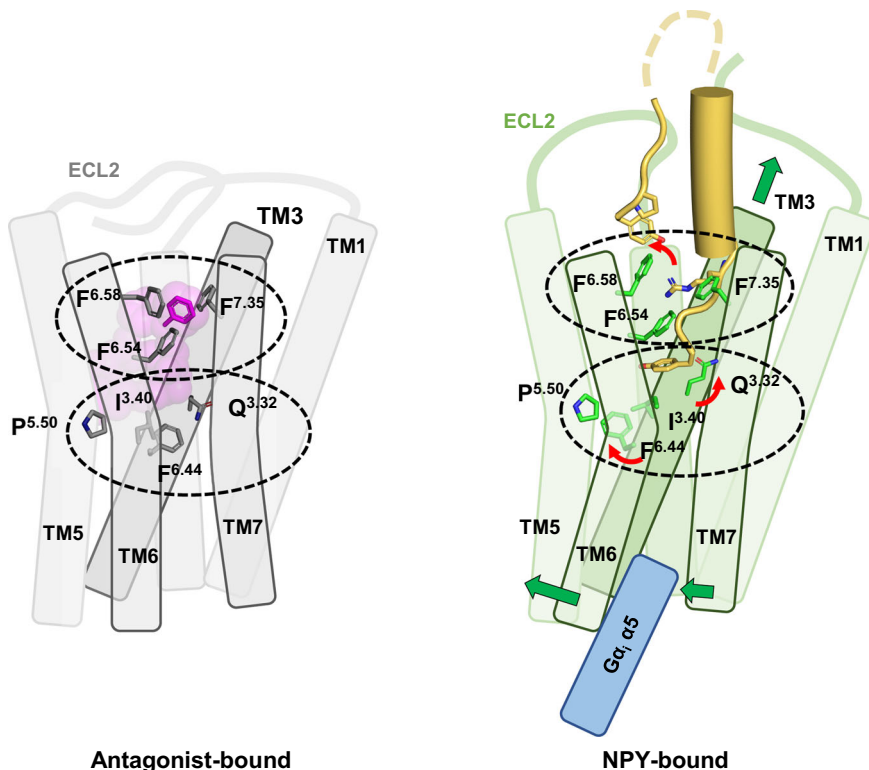


Fig. 6 Mechanism of Y₁R activation by NPY binding. Schematic figures representing antagonist-bound (left) and NPY-bound (right) Y₁R are shown. Two key regions for Y₁R activation are indicated by dashed ellipses. The three phenylalanine residues at TM6 and TM7, and Q120^{3.32}, I128^{3.40}, P223^{5.50}, and F272^{6.44} in the connector region are shown in stick representation. The three phenylalanine residues participate in antagonist binding through π - π interactions, but these interactions are rearranged upon NPY binding. F286^{6.58} flips and forms a new interaction network with Y1 and R33 of NPY. Since F286^{6.58} is not conserved in Y₂R, F286^{6.58}-mediated interactions are Y₁R-selective. Q120^{3.32}, I128^{3.40} and F272^{6.44} show rotamer changes upon NPY binding. A series of these changes upon NPY binding pulls TM3 upward and causes outward movement of the cytoplasmic region of TM6.

tag was cleaved by TEV protease (homemade) treatment at 4 °C overnight. The Hitrap Q column (Cytiva) and a gel filtration column were used for further purification. Purified G α_{i1} dissolved in a solution composed of 20 mM Tris-HCl pH 8.5, 50 mM NaCl, 1 mM MgCl₂, and 10 μ M guanosine diphosphate (GDP) was concentrated, snap frozen in liquid nitrogen, and stored at -80 °C until use.

Human G β_1 with a His₆ tag at its N-terminus and G γ_2 with a C68S mutation were co-expressed in Sf9 insect cells. Cells were harvested 72 h after incubation and lysed with lysis buffer (20 mM Tris-HCl pH 8.5, 0.1 mM Tris (2-carboxyethyl) phosphine hydrochloride (TCEP), and protease inhibitors). After centrifugation, the cleared supernatant was loaded onto a Ni-NTA column. The bound protein was eluted with lysis buffer supplemented with 300 mM imidazole after washing with lysis buffer supplemented with 20 mM imidazole. The His₆ tag was cleaved with HRV 3C protease, and the G $\beta\gamma$ complex was further purified using a Hitrap Q column.

For G protein heterotrimer formation, purified G α_{i1} and G $\beta\gamma$ were mixed in a 1:1:1 molar ratio with excess MgCl₂ and GDP. After an hour of incubation on ice, the G $\alpha\beta\gamma$ complex was purified using a gel filtration column equilibrated with a solution composed of 20 mM HEPES pH 7.5, 150 mM NaCl, 1 mM MgCl₂, and 10 μ M GDP. The purified G $\alpha\beta\gamma$ complex was concentrated, snap frozen in liquid nitrogen, and stored at -80 °C until use.

We confirmed that G α_{i1} produced from *E. coli* is still functional using GTP turnover assay (Supplementary Fig. 29). For comparison, we purified G α_{i1} heterotrimer produced from Sf9 insect cells, as previously described²².

Purification of the scFv16. The scFv16 construct was kindly provided by Dr. Kobilka (Stanford University). Purification of scFv16 was performed by the previously described method with slight modifications¹⁹. First, scFv16 with a His₆ tag at its C-terminus was expressed in *Trichoplusia ni* (Hi5) cells. After cell harvesting, the supernatant containing secreted scFv16 was incubated with Ni-NTA resin at 4 °C for 2 h. The resin was washed with buffer (20 mM HEPES pH 7.0, and 150 mM NaCl, 30 mM imidazole), and the bound protein was eluted with the buffer supplemented with an additional 300 mM imidazole. Further purification was performed using a gel filtration column pre-equilibrated with a solution composed of 20 mM HEPES pH 7.0, and 150 mM NaCl. Purified scFv16 was concentrated, snap frozen in liquid nitrogen, and stored at -80 °C until use.

Purification of the NPY-Y₁R-G α_{i1} -scFv16 complex. Purified Y₁R, G α_{i1} heterotrimer, and scFv16 were mixed at a molar ratio of 1:1:1:2 in the presence of excess NPY (GL Biochem, Shanghai, China) and incubated overnight at 4 °C with apyrase (NEB, MA, USA). The sample was then loaded onto a gel filtration column pre-equilibrated with a solution composed of 20 mM HEPES pH 8.0, 150 mM NaCl, 0.01% GDN, and 2 μ M NPY. The purified NPY-Y₁R-G α_{i1} -scFv16 complex was concentrated to 10 mg/ml and used for cryo-EM grid preparation.

Cryo-EM grid preparation and data collection. An aliquot (3.5 μ l) of purified NPY-Y₁R-G α_{i1} -scFv16 complex was applied onto a glow-discharged holey carbon grid (Quantifoil R1.2/1.3, 300 mesh). The grids were blotted for 5 s at 12 °C and 100% humidity and plunge-frozen in liquid ethane using a Vitrobot Mark IV (Thermo Fisher Scientific, USA) at Center for Macromolecular and Cell imaging of Seoul National University (SNU CMCI). Grids were initially screened with the FEI Glacios (Thermo Fisher Scientific, USA) at SNU CMCI, equipped with a Falcon 4 detector. Images were acquired on a 300-kV Titan Krios (Thermo Fisher Scientific, USA) at Korea Basic Science Institute, equipped with a Falcon 3EC direct electron detector. Movies were recorded in counting mode at a magnification of $\times 161,850$ (corresponding to a calibrated pixel size of 0.865 Å) and a defocus range of -1.25 to -2.75 μ m. A total of 4965 movies were collected, each comprising 40 frames, with a total dose of 40 electrons per Å². A detailed description of the cryo-EM data collection parameters is provided in Supplementary Table 1.

Three-dimensional (3D) reconstruction of NPY-Y₁R-G α_{i1} -scFv16 complex.

Image stack preprocessing was performed using CryoSPARC v. 3.1 (Structura Biotechnology)⁴¹. All movies subjected to beam-induced motion correction using patched-motion correction and contrast transfer function (CTF) parameters for each non-dose-weighted micrograph were determined by patch CTF estimation. After initial particle picking and two-dimensional classification, selected good particles were used for Topaz training⁴². Topaz picking particles (1,300,000 particles) were extracted and subjected to three rounds of heterogeneous refinement. Further heterogeneity classifications were performed by 3D-variability analysis (3DVA)⁴³, focusing on the NPY-Y₁R-G α_{i1} complex without micelles, G α_i AHD, and scFv16 by masking. Clusters with well-resolved density were obtained and used for final map reconstruction by non-uniform refinement⁴⁴. Maps for this

processing have a global nominal resolution of 3.2 Å, based on gold-standard Fourier shell correlation using the 0.143 criteria. To improve the map quality of NPY–Y₁R–G₁₁ complex, we performed the local refinement focusing on the NPY–Y₁R and G₁₁–scFv16 in cryoSPARC v3.2. These local refinements generated the maps at a global nominal resolution of 3.6 Å and 3.1 Å, respectively. Cryo-EM density for ECL2 (176–183, 194–203) and NPY (1–5, 20–36) was clearly observed in the refined map with a mask on NPY–Y₁R. These two local refined maps were combined using “vop maximum” command in UCSF chimera to represent and analyze the NPY–Y₁R–G₁₁ complex⁴⁵. The combined map is represented in Fig. 1a. The local resolution was determined using the cryoSPARC local resolution estimation. Local sharpening was performed by LocSpiral to trace the Y₁R N-terminus (beyond L35^N) and ECL2 region (Supplementary Fig. 6)⁴⁶. No artifacts were observed when compared to the global sharpening map in the other regions.

Model building and refinement. The initial model was obtained by rigid-body-fitting of the structure of inactive Y₁R (PDB ID 5ZBH)¹⁰ and Gα_iβγ and scFv16 from the NTSR1 complex structure (PDB ID 6OS9)²². This initial model was then subjected to iterative rounds of manual rebuilding with COOT and refinement with PHENIX^{47,48}. The geometry of the refined structure was evaluated using the MolProbity⁴⁹. The final model consisting of NPY, Y₁R, Gα_i, Gβ, Gγ, and scFv16 was deposited in the PDB with PDB code 7VGX, and the electron density map was deposited in the EMDB with ID EMD-31979. The refinement statistics are presented in Supplementary Table 1. All molecular graphic figures were prepared using the UCSF Chimera, UCSF ChimeraX, and PyMol v2.4.0^{45,50,51}.

GTP turnover assay. GTP turnover assay was performed using GTPase-Glo assay kit (Promega)²². Purified Y₁R was incubated with NPY for 40 min at room temperature. NPY-bound Y₁R (4 μM) was mixed with 1 μM G₁₁ heterotrimer (containing Gα, produced from *E. coli* or Sf9 cells) in an assay buffer consisting of 20 mM HEPES pH 8.0, 150 mM NaCl, 0.03% DDM, 0.003% CHS, 100 μM TCEP, 5 μM GDP, and 2.5 μM GTP. After incubation for 3 h, reconstituted GTPase-Glo reagent was added to the sample and incubated for 30 min at room temperature. Then, detection reagent was mixed and incubated for 10 min at room temperature. Luminescence was measured using a FlexStation 3 multi-mode microplate reader (Molecular Devices) and data were analyzed by GraphPad Prism 9.2.0.

ELISA-based surface expression assay. HEK293T cells were transfected with each expression plasmid of Y₁R mutants and wild-type. After 48 h of incubation, 4% paraformaldehyde (PFA, T&I) was treated for fixation and washed with 1× PBS. After 30 min of incubation with blocking solution (2.5% bovine serum albumin, Bovogen), rabbit anti-FLAG antibody (Cell signaling Technology, 1:1000 dilution) was then treated for staining and anti-rabbit HRP antibody (Enzo Life Sciences, 1:1000 dilution) was used for detection. After incubation with HRP antibody, TMB solution (ThermoFisher scientific) was added to each well, incubated until blue color was observed. Further reaction was blocked by adding 2 M HCl. The absorbance was detected at 450 nm with FlexStation 3 multi-mode microplate reader. Normalization was carried out by removing TMB substrate solution from the wells and adding Janus Green solution (0.2% w/v, TCL). Further elimination of excess stain was done by washing with milli Q water and adding 0.5 M HCl. Absorbance was read at 595 nm. Normalized expression level of the receptor at the cell surface was calculated by the ratio of the absorbance at 450 and 595 nm (A_{450}/A_{595}). The graphs were plotted using GraphPad Prism 9.2.0.

BRET assay. HEK293T cells were co-transfected with Gα_i-Rluc, Gβ, Gγ, and Y₁R-eYFP constructs at a 1:1:1:5 ratio. Forty-eight hours of post-transfection, cells were detached with PBS supplemented with 20 mM EDTA and evenly spread into white 96-well microplates (SPL). For ligand-induced conditions, various concentrations of NPY were incubated with each Y₁R mutant-transfected group, and Coelenterazine h was added to each well to a final concentration of 5 μM. All BRET data were collected using a Mithras LB940 instrument (Berthold), and graphs were plotted using GraphPad Prism 9.2.0.

Ca²⁺ signaling assay. For the ligand-induced Ca²⁺ assay, HEK293T cells were seeded on 96-well black wall/clear bottom microplate (SPL) in Dulbecco's modified Eagle's medium (Biowest) containing 10% fetal bovine serum (Biowest) and antibiotic-antimycotic (Gibco) 24 h before plasmid transfection. After transfection with the plasmid containing Y₁R constructs, Gα_{Δ6q4dmyr},⁵² Gβ, and Gγ in a 3:1:1:1 ratio, followed by 48 h incubation, cells were stained with Cal-520 (AAT Bioquest, Inc.) in assay buffer (HBSS, 0.1% BSA, 20 mM HEPES pH 7.4). After 2 h, Cal-520-stained cells were washed three times with assay buffer. Intracellular Ca²⁺ influx was measured at Ex/Em = 490/525 nm using the FlexStation 3 multi-mode microplate reader (Molecular Devices). After 30 s of baseline, the ligand was injected to achieve the final concentration. Log (concentration)-response curves, used to estimate EC₅₀, were calculated using GraphPad Prism 9.2.0, by fitting an agonist response curve with a variant slope to the normalized response data.

Calculation of the ligand-binding pocket volume. First, to define the interior of the TM bundle, the receptor structure was aligned along the z-axis by superimposing

a pre-aligned GPCR structure from the OPM database⁵³. Thereafter, a 3D grid was constructed with equispaced points covering the receptor structure. The centers of the TM helices for each discrete z-axis value and the lines connecting the neighboring centers were defined as the lateral boundaries. For helices without a defined center point for a given z-axis value, the (x,y) coordinate of the nearest point was used instead. Next, the upper and lower boundaries of the ligand-binding pocket were defined. The z-axis coordinate of the Cα atom of W^{6.48}, a toggle switch residue, was defined as the lower boundary. TM residues closest to the extracellular region were used to define the upper boundary of the pocket volume. Finally, after removing the grid points causing clashes with protein atoms, the cavity volume was calculated from the number of grid points inside the defined boundaries. The python code for calculating the solvent accessible volume of the ligand-binding pocket is available at https://github.com/seoklab/GPCR_binding_cavity_volume_calculation.

Y₁R-PP homology modeling. The homology model of PP-bound Y₁R was prepared by template-based modeling protocol, GalaxyTBM, using the current NPY-bound Y₁R structure as a template⁵⁴. The initial model was constructed by threading the target sequence on the template structure, followed by energy optimization and additional structure sampling for unreliable local regions. Physics-based optimization method GalaxyRefineComplex refined template-based models⁵⁵. A scoring function optimized for GPCR structure prediction in Galaxy7TM was used⁵⁶.

MD simulation. Missing residues were added to the structure model of the NPY–Y₁R–G₁₁ complex to build an initial model for MD simulation. The AHD domain of G₁₁ was added by aligning the previously reported structure⁵⁷, and the missing residues of Y₁R in the N-terminus (25–34), ECL2 (184–193), ICL2 (247–252), and C-terminus (330–339) were built based on the map with a mask on NPY–Y₁R at a lower threshold. The rest of the N-terminus (2–24) was extended randomly in a position that did not collide with the existing structure.

This study used the CHARMM36(m) force field for proteins and lipids^{58–60}. The TIP3P water model was utilized along with 0.15 M NaCl solution⁶¹. Three independent MD simulations were performed for each system to obtain better sampling and check the convergence. Periodic boundary conditions (PBCs) were employed in all simulations. The van der Waals interactions were smoothly switched off over 10–12 Å by a force-based switching function and the long-range electrostatic interactions were calculated using the particle-mesh Ewald method with a mesh size of ~1 Å⁶². All simulations were performed using the inputs generated by CHARMM-GUI and GROMACS 2018.6 for both equilibration and production with the LINC algorithm^{63–67}. The temperature was maintained using a Nosé-Hoover temperature coupling method with a τ_t of 1 ps⁶⁸. For pressure coupling (1 bar), the semi-isotropic Parrinello–Rahman method with a τ_p of 5 ps and compressibility of 4.5 × 10^{−5} bar^{−1} was used⁶⁹. The constant particle number, volume, and temperature (NVT) dynamics were first applied with a 1-fs time step for 250 ps during the equilibration run. Subsequently, the constant particle number, pressure, and temperature (NPT) ensemble was applied with a 1 fs time step (for 2 ns) and with a 2 fs time step (for 18 ns). During the equilibration, positional and dihedral restraint potentials were applied, and their force constants were gradually reduced. The production run was performed with a 4 fs time step using the hydrogen mass repartitioning technique without any restraint potential⁷⁰. Each system ran about 25 ns/day with 512 CPU cores on NURION in the Korea Institute of Science and Technology Information.

Reporting summary. Further information on research design is available in the Nature Research Reporting Summary linked to this article.

Data availability

Additional data supporting the findings of this work are available as the Supplementary Information, Supplementary Data and Source Data files. The atomic model has been deposited in the Protein Data Bank under accession code 7VGX and the cryo-EM density maps have been deposited in the Electron Microscopy Data Bank under accession code EMD-31979. The structure of inactive Y₁R (PDB ID 5ZBH), Gα_iβγ and scFv16 from the NTSR1 complex structure (PDB ID 6OS9) were used as an initial template to build the NPY–Y₁R–G₁₁ protein model. Structural models used in data analysis were accessed from the Protein Data Bank under the accession codes 5ZBQ (UR-MK299 and Y₁R), 6DDE (μOR, G_i), 7L1U (Oxβ and Ox₂R), 5GLH (ET1 and ET_βR), 7L0Q (NTS and NTSR1), and 7MBX (CCK-8 and CCK1R). Source data are provided with this paper.

Code availability

The python code for calculating the solvent accessible volume of the ligand-binding pocket is available at https://github.com/seoklab/GPCR_binding_cavity_volume_calculation and as a Source Data file.

Received: 2 October 2021; Accepted: 26 January 2022;

Published online: 14 February 2022

References

- Michel, M. C. et al. XVI. International Union of Pharmacology recommendations for the nomenclature of neuropeptide Y, peptide YY, and pancreatic polypeptide receptors. *Pharm. Rev.* **50**, 143–150 (1998).
- Herzog, H. et al. Cloned human neuropeptide Y receptor couples to two different second messenger systems. *Proc. Natl Acad. Sci. USA* **89**, 5794–5798 (1992).
- Kohno, D. & Yada, T. Arcuate NPY neurons sense and integrate peripheral metabolic signals to control feeding. *Neuropeptides* **46**, 315–319 (2012).
- Tasan, R. O. et al. The central and basolateral amygdala are critical sites of neuropeptide Y/Y2 receptor-mediated regulation of anxiety and depression. *J. Neurosci.* **30**, 6282–6290 (2010).
- Gotzsche, C. R. & Woldbye, D. P. The role of NPY in learning and memory. *Neuropeptides* **55**, 79–89 (2016).
- Vahatalo, L. H., Ruohonen, S. T., Ailanen, L. & Savontaus, E. Neuropeptide Y in noradrenergic neurons induces obesity in transgenic mouse models. *Neuropeptides* **55**, 31–37 (2016).
- Farzi, A., Hassan, A. M., Zenz, G. & Holzer, P. Diabesity and mood disorders: Multiple links through the microbiota-gut-brain axis. *Mol. Asp. Med* **66**, 80–93 (2019).
- Zhang, L., Bijker, M. S. & Herzog, H. The neuropeptide Y system: pathophysiological and therapeutic implications in obesity and cancer. *Pharm. Ther.* **131**, 91–113 (2011).
- Monks, S. A., Karagianis, G., Howlett, G. J. & Norton, R. S. Solution structure of human neuropeptide Y. *J. Biomol. NMR* **8**, 379–390 (1996).
- Yang, Z. et al. Structural basis of ligand binding modes at the neuropeptide Y Y(1) receptor. *Nature* **556**, 520–524 (2018).
- Beck-Sickingler, A. G. & Jung, G. Structure-activity relationships of neuropeptide Y analogues with respect to Y1 and Y2 receptors. *Biopolymers* **37**, 123–142 (1995).
- Mentlein, R., Dahms, P., Grandt, D. & Kruger, R. Proteolytic processing of neuropeptide Y and peptide YY by dipeptidyl peptidase IV. *Regul. Pept.* **49**, 133–144 (1993).
- Grandt, D. et al. Novel generation of hormone receptor specificity by amino terminal processing of peptide YY. *Biochem Biophys. Res. Commun.* **186**, 1299–1306 (1992).
- Wieland, H. A., Willim, K. & Doods, H. N. Receptor binding profiles of NPY analogues and fragments in different tissues and cell lines. *Peptides* **16**, 1389–1394 (1995).
- Zheng, H. et al. High-fat intake induced by mu-opioid activation of the nucleus accumbens is inhibited by Y1R-blockade and MC3/4R- stimulation. *Brain Res.* **1350**, 131–138 (2010).
- Yulyaningsih, E., Zhang, L., Herzog, H. & Sainsbury, A. NPY receptors as potential targets for anti-obesity drug development. *Br. J. Pharm.* **163**, 1170–1202 (2011).
- Bhisikar, S. M., Kokare, D. M., Nakhate, K. T., Chopde, C. T. & Subhedar, N. K. Tolerance to ethanol sedation and withdrawal hyper-excitability is mediated via neuropeptide Y Y1 and Y5 receptors. *Life Sci.* **85**, 765–772 (2009).
- Liu, L. et al. NPY1R is a novel peripheral blood marker predictive of metastasis and prognosis in breast cancer patients. *Oncol. Lett.* **9**, 891–896 (2015).
- Maeda, S. et al. Development of an antibody fragment that stabilizes GPCR/G-protein complexes. *Nat. Commun.* **9**, 3712 (2018).
- Dong, M. et al. Structure and dynamics of the active Gs-coupled human secretin receptor. *Nat. Commun.* **11**, 4137 (2020).
- Ballesteros, J. A. & Weinstein, H. Integrated methods for the construction of three-dimensional models and computational probing of structure-function relations in G protein-coupled receptors. *Methods Neurosci.* **25**, 366–428 (1995).
- Kato, H. E. et al. Conformational transitions of a neurotensin receptor 1-G(i1) complex. *Nature* **572**, 80–85 (2019).
- Koehl, A. et al. Structure of the μ -opioid receptor-G(i) protein complex. *Nature* **558**, 547–552 (2018).
- Hong, C. et al. Structures of active-state orexin receptor 2 rationalize peptide and small-molecule agonist recognition and receptor activation. *Nat. Commun.* **12**, 815 (2021).
- Lee, J. H. et al. Solution structure of a new hypothalamic neuropeptide, human hypocretin-2/orexin-B. *Eur. J. Biochem.* **266**, 831–839 (1999).
- Beck-Sickingler, A. G. et al. Complete L-alanine scan of neuropeptide Y reveals ligands binding to Y1 and Y2 receptors with distinguished conformations. *Eur. J. Biochem.* **225**, 947–958 (1994).
- Sautel, M. et al. Neuropeptide Y and the nonpeptide antagonist BIBP 3226 share an overlapping binding site at the human Y1 receptor. *Mol. Pharm.* **50**, 285–292 (1996).
- Sjodin, P. et al. Re-evaluation of receptor-ligand interactions of the human neuropeptide Y receptor Y1: a site-directed mutagenesis study. *Biochem J.* **393**, 161–169 (2006).
- Yin, J. et al. Structure and ligand-binding mechanism of the human OX1 and OX2 orexin receptors. *Nat. Struct. Mol. Biol.* **23**, 293–299 (2016).
- Rappas, M. et al. Comparison of Orexin 1 and Orexin 2 ligand binding modes using X-ray crystallography and computational analysis. *J. Med. Chem.* **63**, 1528–1543 (2020).
- Takasuka, T., Sakurai, T., Goto, K., Furuichi, Y. & Watanabe, T. Human endothelin receptor ETB. Amino acid sequence requirements for super stable complex formation with its ligand. *J. Biol. Chem.* **269**, 7509–7513 (1994).
- Shihoya, W. et al. Crystal structures of human ET(B) receptor provide mechanistic insight into receptor activation and partial activation. *Nat. Commun.* **9**, 4711 (2018).
- Zhang, M. et al. Cryo-EM structure of an activated GPCR-G protein complex in lipid nanodiscs. *Nat. Struct. Mol. Biol.* **28**, 258–267 (2021).
- Mobbs, J. I. et al. Structures of the human cholecystokinin 1 (CCK1) receptor bound to Gs and Gq mimetic proteins provide insight into mechanisms of G protein selectivity. *PLoS Biol.* **19**, e3001295 (2021).
- Schwyzler, R. ACTH: a short introductory review. *Ann. N. Y. Acad. Sci.* **297**, 3–26 (1977).
- Portoghese, P. S. Bivalent ligands and the message-address concept in the design of selective opioid receptor antagonists. *Trends Pharm. Sci.* **10**, 230–235 (1989).
- Stadlbauer, U., Woods, S. C., Langhans, W. & Meyer, U. PYY3-36: Beyond food intake. *Front. Neuroendocrinol.* **38**, 1–11 (2015).
- Cabrele, C., Wieland, H. A., Langer, M., Stidsen, C. E. & Beck-Sickingler, A. G. Y-receptor affinity modulation by the design of pancreatic polypeptide/neuropeptide Y chimera led to Y(5)-receptor ligands with picomolar affinity. *Peptides* **22**, 365–378 (2001).
- Lundell, I. et al. Cloning of a human receptor of the NPY receptor family with high affinity for pancreatic polypeptide and peptide YY. *J. Biol. Chem.* **270**, 29123–29128 (1995).
- Lin, S. et al. Critical role of arcuate Y4 receptors and the melanocortin system in pancreatic polypeptide-induced reduction in food intake in mice. *PLoS ONE* **4**, e8488 (2009).
- Punjani, A., Rubinstein, J. L., Fleet, D. J. & Brubaker, M. A. cryoSPARC: algorithms for rapid unsupervised cryo-EM structure determination. *Nat. Methods* **14**, 290–296 (2017).
- Bepko, T. et al. Positive-unlabeled convolutional neural networks for particle picking in cryo-electron micrographs. *Nat. Methods* **16**, 1153–1160 (2019).
- Punjani, A. & Fleet, D. J. 3D variability analysis: resolving continuous flexibility and discrete heterogeneity from single particle cryo-EM. *J. Struct. Biol.* **213**, 107702 (2021).
- Punjani, A., Zhang, H. & Fleet, D. J. Non-uniform refinement: adaptive regularization improves single-particle cryo-EM reconstruction. *Nat. Methods* **17**, 1214–1221 (2020).
- Petersen, E. F. et al. UCSF Chimera—a visualization system for exploratory research and analysis. *J. Comput. Chem.* **25**, 1605–1612 (2004).
- Kaur, S. et al. Local computational methods to improve the interpretability and analysis of cryo-EM maps. *Nat. Commun.* **12**, 1240 (2021).
- Emsley, P., Lohkamp, B., Scott, W. G. & Cowtan, K. Features and development of Coot. *Acta Crystallogr D* **66**, 486–501 (2010).
- Liebschner, D. et al. Macromolecular structure determination using X-rays, neutrons and electrons: recent developments in Phenix. *Acta Crystallogr D* **75**, 861–877 (2019).
- Williams, C. J. et al. MolProbity: more and better reference data for improved all-atom structure validation. *Protein Sci.* **27**, 293–315 (2018).
- Goddard, T. D. et al. UCSF ChimeraX: meeting modern challenges in visualization and analysis. *Protein Sci.* **27**, 14–25 (2018).
- Schrödinger. The PyMOL Molecular Graphics System, Version 2.4.0, Schrödinger LLC. (2020).
- Kostenis, E. Potentiation of GPCR-signaling via membrane targeting of G protein alpha subunits. *J. Recept Signal Transduct. Res.* **22**, 267–281 (2002).
- Lomize, M. A., Lomize, A. L., Pogozheva, I. D. & Mosberg, H. I. OPM: orientations of proteins in membranes database. *Bioinformatics* **22**, 623–625 (2006).
- Ko, J., Park, H. & Seok, C. GalaxyTBM: template-based modeling by building a reliable core and refining unreliable local regions. *BMC Bioinform.* **13**, 198 (2012).
- Heo, L., Lee, H. & Seok, C. GalaxyRefineComplex: refinement of protein-protein complex model structures driven by interface repacking. *Sci. Rep.* **6**, 32153 (2016).
- Lee, G. R. & Seok, C. Galaxy7TM: flexible GPCR-ligand docking by structure refinement. *Nucleic Acids Res.* **44**, W502–W506 (2016).
- Kang, Y. et al. Cryo-EM structure of human rhodopsin bound to an inhibitory G protein. *Nature* **558**, 553–558 (2018).
- Huang, J. et al. CHARMM36m: an improved force field for folded and intrinsically disordered proteins. *Nat. Methods* **14**, 71–73 (2017).

59. Klauda, J. B., Monje, V., Kim, T. & Im, W. Improving the CHARMM force field for polyunsaturated fatty acid chains. *J. Phys. Chem. B* **116**, 9424–9431 (2012).
60. Klauda, J. B. et al. Update of the CHARMM all-atom additive force field for lipids: validation on six lipid types. *J. Phys. Chem. B* **114**, 7830–7843 (2010).
61. Jorgensen, W. L., Chandrasekhar, J., Madura, J. D., Impey, R. W. & Klein, M. L. Comparison of simple potential functions for simulating liquid water. *J. Chem. Phys.* **79**, 926–935 (1983).
62. Essmann, U. et al. A smooth particle Mesh Ewald method. *J. Chem. Phys.* **103**, 8577–8593 (1995).
63. Lee, J. et al. CHARMM-GUI input generator for NAMD, GROMACS, AMBER, OpenMM, and CHARMM/OpenMM simulations using the CHARMM36 additive force field. *J. Chem. Theory Comput.* **12**, 405–413 (2016).
64. Van Der Spoel, D. et al. GROMACS: fast, flexible, and free. *J. Comput. Chem.* **26**, 1701–1718 (2005).
65. Hess, B., Bekker, H., Berendsen, H. J. C. & Fraaije, J. G. E. M. LINCS: a linear constraint solver for molecular simulations. *J. Comput. Chem.* **18**, 1463–1472 (1997).
66. Jo, S., Lim, J. B., Klauda, J. B. & Im, W. CHARMM-GUI membrane builder for mixed bilayers and its application to yeast membranes. *Biophys. J.* **97**, 50–58 (2009).
67. Jo, S., Kim, T. & Im, W. Automated builder and database of protein/membrane complexes for molecular dynamics simulations. *PLoS ONE* **2**, e880 (2007).
68. Hoover, W. G. Canonical dynamics: equilibrium phase-space distributions. *Phys. Rev. A* **31**, 1695–1697 (1985).
69. Parrinello, M. & Rahman, A. Polymorphic transitions in single-crystals—a new molecular-dynamics Method. *J. Appl. Phys.* **52**, 7182–7190 (1981).
70. Hopkins, C. W., Le Grand, S., Walker, R. C. & Roitberg, A. E. Long-time-step molecular dynamics through hydrogen mass repartitioning. *J. Chem. Theory Comput.* **11**, 1864–1874 (2015).

Acknowledgements

This work was supported by the Creative-Pioneering Researchers Program through Seoul National University (H.-J.C.), the National Research Foundation of Korea funded by the Korean government (NRF-2020R1A2C2003783 and NRF-2019M3E5D6063903 to H.-J.C.), and National Science Foundation, USA (MCB-2111728 to W.I.). This work was also supported by Korea Basic Science Institute grant (2020R1A6C101A183 to H.-J.C.) and the Korea Basic Science Institute under the R&D program (Project No. C140440 to H.-J.C. and H.J.) supervised by the Ministry of Science and ICT. We thank Dr. Brian Kobilka (Stanford University) for providing the scFv16 construct, Chul Won Choi and Jungnam Bae (Seoul National University) for supporting grid preparation, Junsun Park and Dr. Soung-Hun Roh (Seoul National University) for providing materials and methods for grid screening. We also thank Dr. Bum Han Ryu (Institute for Basic Science (IBS), Korea) and Dr. Jin Seok Choi (KAIST Analysis Center for Research Advancement (KARA), Korea) for supporting grid screening at IBS and KARA cryo-EM facilities, respectively, and Global Science experimental Data hub Center (GSDC) at Korea Insti-

tute of Science and Technology Information (KISTI) and the data analysis hub, Olaf at the IBS Research Solution Center for computing resources.

Author contributions

C.P. and J.K. contributed equally to this work. C.P. purified the NPY-Y₁R-G₁₁-scFv16 complex. J.K. collected and processed cryo-EM data with help from H.J. and I.B. C.P. and J.K. determined and refined the complex structure. S.B.K. performed cell-based assays including surface ELISA, BRET assays, and Ca²⁺ assays with help from J.K., S.A.K., and T.-Y.Y. Y.K.C. and W.I. performed MD simulations and H.W. and C.S. calculated the volume of ligand-binding pockets and generated a homology model of PP-bound Y₄R. H.K. purified G₁₁ heterotrimer and scFv16. H.-J.C. conceived and directed the study. C.P., J.K., I.B., and H.-J.C. wrote the manuscript with contributions from all authors.

Competing interests

The authors declare no competing interests.

Additional information

Supplementary information The online version contains supplementary material available at <https://doi.org/10.1038/s41467-022-28510-6>.

Correspondence and requests for materials should be addressed to Hee-Jung Choi.

Peer review information *Nature Communications* thanks Cheng Zhang and the other, anonymous, reviewer(s) for their contribution to the peer review of this work. Peer reviewer reports are available.

Reprints and permission information is available at <http://www.nature.com/reprints>

Publisher's note Springer Nature remains neutral with regard to jurisdictional claims in published maps and institutional affiliations.



Open Access This article is licensed under a Creative Commons Attribution 4.0 International License, which permits use, sharing, adaptation, distribution and reproduction in any medium or format, as long as you give appropriate credit to the original author(s) and the source, provide a link to the Creative Commons license, and indicate if changes were made. The images or other third party material in this article are included in the article's Creative Commons license, unless indicated otherwise in a credit line to the material. If material is not included in the article's Creative Commons license and your intended use is not permitted by statutory regulation or exceeds the permitted use, you will need to obtain permission directly from the copyright holder. To view a copy of this license, visit <http://creativecommons.org/licenses/by/4.0/>.

© The Author(s) 2022, corrected publication 2022